Journal of Sound and Vibration 329 (2010) 1809–1822

Contents lists available at ScienceDirect

Journal of Sound and Vibration

journal homepage: www.elsevier.com/locate/jsvi

Frequency band structure and absorption predictions for multi-periodic acoustic composites

Chang-Yong Lee [a], Michael J. Leamy [a,*], Jason H. Nadler [b]

[a] School of Mechanical Engineering, Georgia Institute of Technology, Atlanta, Georgia 30332, USA
[b] Georgia Tech Research Institute (GTRI), Georgia Institute of Technology, Atlanta, Georgia 30332, USA

ARTICLE INFO

Article history:
Received 13 July 2009
Received in revised form
16 November 2009
Accepted 24 November 2009
Handling Editor: A.V. Metrikine
Available online 22 December 2009

ABSTRACT

This article introduces a computational framework for studying frequency band structure and absorption behavior in multi-periodic acoustic composite structures. Herein, multi-periodic acoustic composite structures are defined as periodically-layered acoustic media wherein each layer is composed of periodically-repeated fluid unit cells, especially those arising from the study of porous materials. Hence, at least two periodic scales (microscopic and mesoscopic, respectively) comprise the macroscopic acoustic composite media. Exploitation of the multi-periodicity allows for efficient generation of dispersion and absorption curves via the conventional multi-scale asymptotic method (for homogenizing the mesoscale) coupled to the acoustic transfer matrix methods (for the macroscale). The combined computational framework results in a single analysis procedure for evaluating complex dispersion relationships and acoustic absorption. The dispersion curves can be used to reveal frequency stop bands wherein the wave vector is highly imaginary—i.e., plane waves experience rapid attenuation. They can also be used to reinterpret classical absorption curves. The framework is applied to four multi-periodic acoustic composite structures in order to demonstrate the framework's utility and to reveal novel properties, particularly those which can be influenced by design of the mesoscopic unit cell.

1. Introduction

Porous materials have demonstrated excellent potential for use as high strength, low-weight structural materials; as superior noise and energy absorption materials; and in high-temperature applications [1]. Due to these properties, research attention devoted to theoretical [2–9,11,13,15–17,52] and computational [10,12,14,18–29] formulations for predicting and controlling their material and acoustic properties have received considerable attention in the past several decades. However, little research attention has been paid to synthetically-derived acoustic composite structures, especially those derived from layering of periodic porous media.

In this work, techniques from the studies of wave propagation in periodic *elastic* media (see the pioneering work of Floquet [30] and Bloch [31]) and of acoustic wave propagation in layered media with arbitrary succession of fluid, elastic, and porous layers (see the early work of Thompson [32] (corrected by Haskell [33])) are applied to analyze the dispersion behavior of multi-periodic acoustic composite structures. In general, the dispersion curves exhibit (a) stop-band (or band-gap) ranges, in which waves are not allowed to propagate through the structures, and (b) pass-band ones, in which waves

* Corresponding author. Tel.: +1 404 385 2828; fax: +1 404 894 8496.
E-mail address: michael.leamy@me.gatech.edu (M.J. Leamy).

0022-460X/$ - see front matter © 2009 Elsevier Ltd. All rights reserved.
doi:10.1016/j.jsv.2009.11.030

are permitted. Reviewing the existing literature, there is a tremendous amount of work done on developing analytical and numerical approaches for predicting and control wave propagations in periodic media made of photonic, sonic, and phononic crystals (see, e.g., Refs. [34–36] for a review). Several studies are also conducted on wave propagation in a periodically layered composite structures made of different material properties [37–45]. However, since most of the established approaches explicitly assume no or prescribed attenuation, the reviewed methods are not suitable for determining and tailoring the wave propagation characteristics of arbitrary acoustic composite structures, which have frequency-dependent dissipation properties due to viscothermal effects arising at the pore walls.

The main objective of this paper is to then present a consistent and general approach for predicting wave propagation behavior in the fluid-filled spaces of multi-periodic acoustic composite structures. These structures will be composed of N repetitions of a single n-layered mesoscopic unit cell containing porous acoustic materials at the microscopic level (see Fig. 1). To do this, we begin our presentation in Section 2 by briefly reviewing a frequency-domain mathematical and numerical procedures suitable for estimating the effective wave number ($k_{eff}^{(i)}$) and impedance ($Z_{eff}^{(i)}$) characteristics of the ith layer in the Kth mesoscopic unit cell, termed the multi-scale asymptotic method (MAM) [4–8,10–12,14,19,21] and the hybrid numerical method (HNM) [24,25,27–29]. The MAM is used to derive a frequency-dependent set of partial differential equations and associated boundary conditions for viscous and thermal responses from knowledge of the micro-scale physics and geometry in a representative unit fluid cell (UFC). The HNM is an alternative method used to avoid significant computational burden and convergence issues generated in direct computation at each frequency of interest. In HNM, one calculates *static* acoustic parameters for use as input data in explicit expressions for frequency-dependent effective density ($\rho_{eff}^{(i)}$) and compressibility ($\chi_{eff}^{(i)}$) proposed by Pride et al. [16] and Lafarge [17], respectively, in an elaboration of the original and important steps made by Johnson et al. [9] for viscous effects, and Allard and Champoux for thermal effects [13]. A recent and detailed account of the general theory and (HNM) modeling of both functions of frequency may be found in [52] Part 2, Chapter 6. Subsequently, the effective variables are taken to estimate complex-valued effective wave number ($k_{eff}^{(i)}$) and impedance ($Z_{eff}^{(i)}$) as the meso-scale parameters to represent acoustic properties of the ith layer.

In Section 3 the acoustic transfer matrix method (ATMM) is used to study plane wave propagation in the stratified medium, either finite or infinite. Section 3.1 employs the ATMM in conjunction with the Floquet–Bloch theorem (termed herein infinite ATMM) to derive the macroscopic dispersion curves of the infinite periodic structure case ($N\to\infty$) composed of an arbitrary n-layered mesoscopic unit cell. To overcome the limitations of the infinite approach (namely, the requirement of infinite layers), Section 3.2 describes a second analysis approach applicable to *finite* periodic structures consisting of N layers, termed herein the finite ATMM. In Section 4, several numerical examples are illustrated. First, we estimate and then collect static acoustic parameters for five UFC cases represented by three close-packed and two

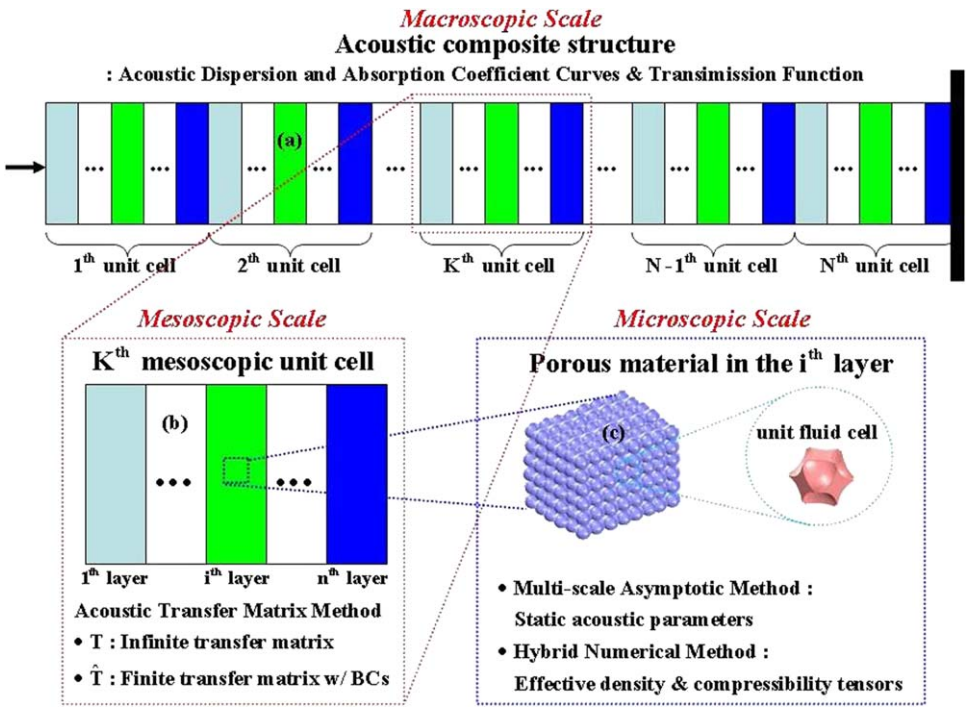

Fig. 1. Three spatial scale descriptions and associated applicable methods of (a) the N periodically acoustic composite structure consisting, (b) a single n-layered mesoscopic unit cell, which are composed of arbitrarily chosen, and (c) porous material properties.

open-packed sphere arrangements at the micro-scale level. Second, based on the above information, we investigate the macro-scale dispersion relations for four acoustic composite structures composed of bi-layered mesoscopic unit cells using the infinite ATMM. We compare the general shapes of the transmission function's amplitudes and acoustic absorption curves for four finite $N\times 2$ structures with estimated dispersion relations, where $N=1,3,5,7,10$ denotes the finite number of mesoscopic unit cells present, and 2 denotes the two layers in each mesoscopic cell. Finally we explore the close relationship between acoustic absorption and frequency band structure.

2. Mutli-scale asymptotic and hybrid numerical methods

2.1. Multi-scale asymptotic method

The multi-scale asymptotic method (MAM) [4–8,10–12,14,19,21] is utilized herein to derive the microscopic boundary value problems whose solutions, once averaged, determine the effective density and compressibility. It assumes the existence of a distinct scale separation between two types of spatial variations (slow variations described by x and rapid variations described by $y=\varepsilon^{-1}x$). Here the small parameter $\varepsilon=l/d\ll 1$ is a scale ratio of the characteristic UFC length l at the micro-scale level and the characteristic layer length d at the meso-scale level. Using the knowledge of the micro-scale pore's physics and geometries, MAM enables one to determine frequency-dependent meso-scale material properties inside the ith layer: frequency-dependent effective density ($\rho_{eff}^{(i)}$) and compressibility ($\chi_{eff}^{(i)}$). These effective properties in-turn yield the layer's complex-valued effective wave number ($k_{eff}^{(i)}$) and acoustic impedance ($Z_{eff}^{(i)}$).

First, consider the acoustic fluid motion inside the ith layer composed of a rigid porous material. It is described by the following set of harmonic viscous-thermal governing equations and associated boundary conditions:

- In the viscothermal fluid flow,

$$\frac{p^{(i)}}{P_0}=\frac{\rho^{(i)}}{\rho_0}+\frac{\tau^{(i)}}{T_0}\quad\text{(state equation of a perfect gas)},\tag{1}$$

$$\rho_0 \mathrm{i}\omega\mathbf{u}^{(i)}=-\nabla p^{(i)}+(\lambda+\mu)\nabla(\nabla\cdot\mathbf{u}^{(i)})+\mu\Delta\mathbf{u}^{(i)}$$
$$\mathrm{i}\omega\frac{\rho^{(i)}}{\rho_0}=-\nabla\cdot\mathbf{u}^{(i)}\qquad\text{(momentum and mass balance)},\tag{2a,b}$$

$$\rho_0\mathrm{i}\omega C_p\tau^{(i)}=\mathrm{i}\omega p^{(i)}+K\Delta\tau^{(i)}\quad\text{(energy balance)},\tag{3}$$

- On the fluid–solid interface,

$$\mathbf{u}^{(i)}=0\quad\text{and}\quad\tau^{(i)}=0(\text{no}-\text{slip and isothermal conditions})\tag{4a,b}$$

where ∇ and Δ denotes the gradient and Laplacian operators. Here P_0, ρ_0, and T_0 denote the pressure, density, and temperature of the air at the rest, while $\mathbf{u}^{(i)}$, $\rho^{(i)}$, and $\tau^{(i)}$ denote the fluid velocity, pressure and temperature variations. In addition, the shear and bulk viscosities, specific heat at constant pressure, and heat conductivity are denoted, respectively, by μ, λ, C_P, and K. Following the standard MAM procedure, all solution variables and the differential operators in (1)–(4) are considered as functions of both their mesoscopic and microscopic variations via power series involving ε:

$$\mathbf{u}^{(i)}=\mathbf{u}^{0(i)}(x,y)+\varepsilon\mathbf{u}^{1(i)}(x,y)+\varepsilon^2\mathbf{u}^{2(i)}(x,y)+\cdots$$
$$p^{(i)}=p^{0(i)}(x,y)+\varepsilon p^{1(i)}(x,y)+\varepsilon^2 p^{2(i)}(x,y)+\cdots$$
$$\tau^{(i)}=\tau^{0(i)}(x,y)+\varepsilon\tau^{1(i)}(x,y)+\varepsilon^2\tau^{2(i)}(x,y)+\cdots\tag{5}$$

and

$$\nabla=\nabla_x+\frac{1}{\varepsilon}\nabla_y,\quad \Delta=\Delta_x+\frac{2}{\varepsilon}\Delta_{xy}+\frac{1}{\varepsilon^2}\Delta_y\tag{6}$$

Substituting (5) and (6) into (1)–(4) and retaining the leading terms, the following set of micro-scale partial differential equations and associated boundary conditions is obtained:

- Momentum equation with no-slip boundaries

$$\rho_0\mathrm{i}\omega\mathbf{u}^{0(i)}-\mu\Delta_y\mathbf{u}^{0(i)}+\nabla_y p^{1(i)}=-\nabla_x p^{0(i)}$$
$$\nabla_y\cdot\mathbf{u}^{0(i)}=0\qquad\text{in }\Omega_f^{(i)}\tag{7}$$

$$\mathbf{u}^{0(i)}=0\quad\text{on }\Gamma^{(i)}(\mathbf{u}^{0(i)}\&p^{1(i)}:\ \Omega^{(i)}\text{—periodic})$$

- Energy equation with isothermal boundaries

$$\rho_0 \mathrm{i}\omega C_p \tau^{0(i)} - K \Delta_y \tau^{0(i)} = \mathrm{i}\omega p^{0(i)} \text{in } \Omega_f^{(i)}$$

$$\tau^{0(i)} = 0 \quad \text{on } \Gamma^{(i)} \ (\tau^{0(i)} : \Omega^{(i)} \text{—periodic}) \tag{8}$$

Here $\Omega^{(i)}$ denotes the entire cell volume, $\Omega_f^{(i)}$ denotes the fluid-filled spaces, and $\Gamma^{(i)}$ denotes the fluid–solid interface. Knowing the microscopic solutions $\mathbf{u}^{0(i)}$ and $\tau^{0(i)}$ of the above micro-scale problems, one obtains the effective density ($\rho_{eff}^{(i)}$) and compressibility ($\chi_{eff}^{(i)}$) in the ith layer by averaging over the UFC. See our previous work [29] for a complete discussion.

2.2. Hybrid numerical method

The formulation represented in (7) and (8) can still present difficulties in obtaining a numerical solution due to the need for full solutions at each frequency and accompanying numerical convergence issues in the three-dimensional case. Recently, an alternative, analytic-based approach has been introduced [24,25,27–29] (termed herein the HNM). The main advantage of this approach is the need to solve only three *static* (zero angular frequency) problems instead of dynamic problems such as (7) and (8). Namely, following the methodology introduced by Lafarge et al. [18], one can assume, at a given frequency, three appropriate solution forms of the micro-scale velocity, pressure and temperature distributions as follows:

$$\mu \mathbf{u}^{0(i)}(x,y) = -\mathbf{k}^{(i)}(y,\omega) \cdot \nabla_x p^{0(i)}(x), p^{1(i)}(x,y) = -\boldsymbol{\pi}^{(i)}(y,\omega) \cdot \nabla_x p^{0(i)}(x) + \hat{p}^{1(i)}(x) \tag{9a,b}$$

and

$$K \tau^{0(i)}(x,y) = k'^{(i)}(y,\omega) \mathrm{i}\omega p^{0(i)}(x) \tag{10}$$

where $\mathbf{k}^{(i)}$ and $k'^{(i)}$ denote the micro-scale dynamic viscous and thermal permeability functions. Note in arriving at these expressions ($p^{1(i)}$) is decomposed into a mean part ($\hat{p}^{1(i)}$) and a deviatoric part ($\boldsymbol{\pi}^{(i)}$) having zero mean value. Substituting (9) and (10) into (7) and (8) and addressing the relevance (in a high-frequency limit) between electrical conduction and sound propagation [12,17,27–29,46] yield the following set of three different static problems to be solved for computing seven static parameters (see below Eqs. (14) and (15)) of the porous acoustic material inside the ith layer:

- Viscous: Stokes equation with no-slip boundaries

$$\begin{aligned} \nabla_y \boldsymbol{\pi}^{(i)} - \Delta_y \mathbf{k}^{(i)} &= I \\ \nabla_y \cdot \mathbf{k}^{(i)} &= 0 \end{aligned} \quad \text{in } \Omega_f^{(i)} \tag{11}$$

$$\mathbf{k}^{(i)} = 0 \quad \text{on } \Gamma^{(i)} \ (\mathbf{k}^{(i)} \text{ and } \boldsymbol{\pi}^{(i)} : \Omega^{(i)} \text{—periodic})$$

- Thermal: heat equation with isothermal boundaries

$$-\Delta_y k'^{(i)} = 1 \quad \text{in } \Omega_f^{(i)} \tag{12}$$

$$k'^{(i)} = 0 \quad \text{on } \Gamma^{(i)} \ (k'^{(i)} : \Omega^{(i)} \text{—periodic})$$

- Electrical: conduction problem with insulation boundaries

$$\nabla \cdot \mathbf{E}^{(i)} = 0 \quad \text{with } \mathbf{E}^{(i)} = -\nabla_y \boldsymbol{\varphi}^{(i)} + \mathbf{I} \quad \text{in } \Omega_f^{(i)} \tag{13}$$

$$\mathbf{E}^{(i)} \cdot \mathbf{n} = 0 \quad \text{on } \Gamma^{(i)} \ (\varphi^{(i)} : \Omega^{(i)} \text{—periodic})$$

Here $E_{\alpha\beta}^{(i)}$ ($\alpha, \beta = 1, 2, 3$) represents the scaled electric field, $\boldsymbol{\varphi}^{(i)}$ the deviatoric part of the electric potential, and $\mathbf{n}$ the unit outward normal vector from the pore region. In addition, $\mathbf{I}$ denotes a 3×3 identity matrix composed of three unit vectors ($\mathbf{e}$) directed along a global coordinate system. In particular, the static parameters can be also reduced from tensor-based values to scalars by referring to their own symmetry properties in static regime [47]. These parameters are taken to be the static viscous and thermal permeability ($\hat{k}_0^{(i)}, \hat{k}_0^{'(i)}$), the tortuosity factor ($\alpha_\infty^{(i)}$), the static viscous and thermal tortuosity ($\alpha_0^{(i)}, \alpha_0^{'(i)}$), and the viscous and thermal characteristic lengths ($\Lambda^{(i)}, \Lambda'^{(i)}$), which are simply calculated by the following standard definitions [9,17]:

$$\hat{\mathbf{k}}_0^{(i)} = \phi^{(i)} \langle \mathbf{k}^{(i)} \rangle = \hat{k}_0^{(i)}, \quad \hat{k}_0^{'(i)} = \phi^{(i)} \langle k'^{(i)} \rangle, \quad \boldsymbol{\alpha}_\infty^{(i)-1} = \langle \mathbf{E}^{(i)} \rangle = \alpha_\infty^{(i)-1}, \tag{14}$$

and

$$\alpha_0^{(i)} = \frac{\langle \mathbf{k}^{(i)2} \rangle}{\langle \mathbf{k}^{(i)} \rangle^2}, \quad \alpha_0^{'(i)} = \frac{\langle k'^{(i)2} \rangle}{\langle k'^{(i)} \rangle^2}, \quad \Lambda^{(i)} = 2\frac{\int\int\int_{\Omega^{(i)}} \mathbf{E}^{(i)2} \, \mathrm{d}\Omega^{(i)}}{\int\int_{\Gamma^{(i)}} \mathbf{E}^{(i)2} \, \mathrm{d}\Gamma^{(i)}}, \quad \Lambda'^{(i)} = 2\frac{\int\int\int_{\Omega^{(i)}} \mathrm{d}\Omega^{(i)}}{\int\int_{\Gamma^{(i)}} \mathrm{d}\Gamma^{(i)}} \tag{15}$$

with $\phi^{(i)}=\Omega_f^{(i)}/\Omega^{(i)}$ and $\langle\bullet\rangle=\int_{\Omega^{(i)}}\bullet \mathrm{d}\Omega^{(i)}/\Omega_f^{(i)}$. Here subscripts 0 and ∞ represent quantities evaluated at $\omega=0$ and the high frequency limit case, respectively. These then serve as input data in explicit expressions for the ith frequency-dependent effective density ($\rho_{eff}^{(i)}$) and compressibility ($\chi_{eff}^{(i)}$) variables proposed by Pride et al. [16] and Lafarge [17], respectively

$$\mathrm{i}\omega\rho_{eff}^{(i)}\langle\mathbf{u}^{0(i)}\rangle=-\nabla_x p^{0(i)} \quad \text{and} \quad \mathrm{i}\omega\chi_{eff}^{(i)}p^{0(i)}=-\nabla_x\cdot\langle\mathbf{u}^{0(i)}\rangle \tag{16a,b}$$

where

$$\rho_{eff}^{(i)}=\rho_0\alpha_\infty^{(i)}\left[1+\frac{f^{(i)}(\zeta^{(i)})}{\mathrm{i}\zeta^{(i)}}\right] \quad \text{and} \quad \chi_{eff}^{(i)}=\frac{1}{\gamma P_0}\left\{\gamma-(\gamma-1)\left[1+\frac{f'^{(i)}(\zeta'^{(i)})}{\mathrm{i}\zeta'^{(i)}}\right]^{-1}\right\} \tag{17a,b}$$

with

$$f^{(i)}(\zeta^{(i)})=1-q^{(i)}+q^{(i)}\sqrt{1+\mathrm{i}\zeta^{(i)}\frac{M^{(i)}}{2q^{(i)2}}}, \quad f'^{(i)}(\zeta'^{(i)})=1-q'^{(i)}+q'^{(i)}\sqrt{1+\mathrm{i}\zeta'^{(i)}\frac{M'^{(i)}}{2q'^{(i)2}}} \tag{18}$$

$$\zeta^{(i)}=\frac{\omega\rho_0\hat{k}_0^{(i)}\alpha_\infty^{(i)}}{\mu\phi^{(i)}}, \quad \zeta'^{(i)}=\frac{\omega\rho_0\hat{k}_0'^{(i)}Pr}{\mu\phi^{(i)}}, \quad M^{(i)}=\frac{8\hat{k}_0^{(i)}\alpha_\infty^{(i)}}{\Lambda^{(i)2}\phi^{(i)}}, \quad M'^{(i)}=\frac{8\hat{k}_0'^{(i)}}{\Lambda'^{(i)2}\phi^{(i)}} \tag{19}$$

and

$$q^{(i)}=\frac{M^{(i)}}{4\left(\frac{\alpha_0^{(i)}}{\alpha_\infty^{(i)}}-1\right)}, \quad q'^{(i)}=\frac{M'^{(i)}}{4(\alpha_0'^{(i)}-1)} \tag{20}$$

where $f^{(i)}$ and $f'^{(i)}$ represent the ith dimensionless viscous and thermal shape functions of each angular frequency ($\zeta^{(i)},\zeta'^{(i)}$), and $M^{(i)}$ and $M'^{(i)}$ the corresponding dimensionless viscous and thermal shape factors, respectively, while $q^{(i)}$ and $q'^{(i)}$ associated dimensionless supplementary parameters. Using the definitions of the two effective parameters (16), one can derive the acoustic wave equation as follows:

$$\nabla_x\cdot\left(\frac{1}{\rho_{eff}^{(i)}}\nabla_x p^{0(i)}\right)+\omega^2\chi_{eff}^{(i)}p^{0(i)}=0 \tag{21}$$

Finally, the effective wave number ($k_{eff}^{(i)}$) and impedance ($Z_{eff}^{(i)}$) are defined as,

$$k_{eff}^{(i)}=\omega\sqrt{\rho_{eff}^{(i)}\chi_{eff}^{(i)}} \quad \text{and} \quad Z_{eff}^{(i)}=\frac{1}{\phi^{(i)}}\sqrt{\frac{\rho_{eff}^{(i)}}{\chi_{eff}^{(i)}}} \tag{22a,b}$$

3. Acoustic transfer matrix formulation

We next employ the acoustic transfer matrix method (ATMM) for studying frequency band structure in multi-periodic acoustic composite structures. The ATMM is given in an explicit and elegant one-dimensional analytic form. Note that for layered *elastic* composite structures, an equivalent method, termed the elastic transfer matrix method (ETMM), was previously introduced by Esquivel-Sirvent and Cocoletzi in the infinite case [40], Cao and Qi in the finite case [42], and recently Hussein et al. in both cases [43]. However, unlike the existing ETMM method, the ATMM is especially suitable to study dissipative wave propagation characteristics in the one-dimensionally periodic, layered acoustic composite composed of dispersive properties created in rigid porous materials in the infinite (Section 3.1) and finite (Section 3.2) cases.

3.1. Infinite periodic case

Let us first consider the one-dimensional configuration of the infinite, n-layered mesoscopic unit cell composed of different porous material properties and thicknesses (Fig. 2). As sketched in Fig. 2, acoustic properties of the ith layer in the mesoscopic unit cell are explicitly represented by frequency-dependent and complex-valued effective wave number ($k_{eff}^{(i)}$) and impedance ($Z_{eff}^{(i)}$), porosity ($\phi^{(i)}$), and material thickness ($d^{(i)}$), obtained from the previous section (see Section 3.2).

The governing equation for harmonic plane wave propagation along the x-axis can be rewritten from (21):

$$\frac{1}{\rho_{eff}^{(i)}}\frac{d^2p^{(i)}}{dx^2}+\omega^2\chi_{eff}^{(i)}p^{(i)}=0 \tag{23}$$

Note that here and throughout the rest of the acoustic transfer matrix development, superscript 0 in (23) is omitted for convenience. Two boundary conditions have to be satisfied at each layer interface: (i) continuity of the pressure p and

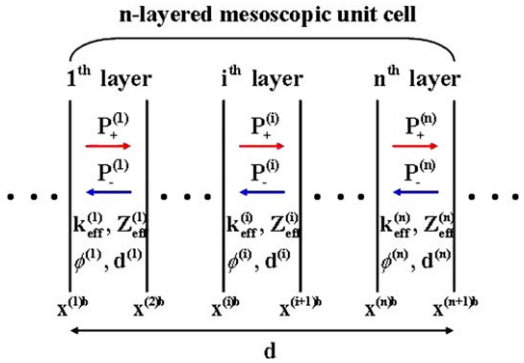

Fig. 2. Mesoscopic unit cell consisting of n sub-layers. Acoustic property and thickness of the ith layer are denoted by $(\bullet)^{(i)}$, while left and right interface boundaries of the ith layer are identified by $(\bullet)^{(i)b}$ and $(\bullet)^{(i+1)b}$, respectively.

(ii) continuity of the effective velocity u_{eff} (equally ϕu). These boundary conditions are similar to the impedance tube method (ITM) [15,48–50] used to calculate the acoustic absorption coefficient α. Without loss of generality, the solution of Eq. (23) in the ith layer is assumed as a superposition of forward and backward traveling waves:

$$p^{(i)}(x) = P_+^{(i)} e^{-ik_{eff}^{(i)}x} + P_-^{(i)} e^{ik_{eff}^{(i)}x} \tag{24}$$

Substituting (22) and (24) into (16a), the effective velocity component can be given in terms of $P_+^{(i)}$ and $P_-^{(i)}$:

$$u_{eff}^{(i)}(x) = \phi^{(i)} u^{(i)}(x) = \phi^{(i)}[U_+^{(i)} e^{-ik_{eff}^{(i)}x} + U_-^{(i)} e^{ik_{eff}^{(i)}x}] = \frac{P_+^{(i)}}{Z_{eff}^{(i)}} e^{-ik_{eff}^{(i)}x} - \frac{P_-^{(i)}}{Z_{eff}^{(i)}} e^{ik_{eff}^{(i)}x} \tag{25}$$

For convenience, (24) and (25) can be simply rewritten in the following matrix form as

$$\begin{Bmatrix} p^{(i)}(x) \\ u_{eff}^{(i)}(x) \end{Bmatrix} = \begin{bmatrix} 1 & 1 \\ \dfrac{1}{Z_{eff}^{(i)}} & -\dfrac{1}{Z_{eff}^{(i)}} \end{bmatrix} \begin{Bmatrix} P_+^{(i)} e^{-ik_{eff}^{(i)}x} \\ P_-^{(i)} e^{ik_{eff}^{(i)}x} \end{Bmatrix} = \mathbf{B}_{(i)} \begin{Bmatrix} P_+^{(i)} e^{-ik_{eff}^{(i)}x} \\ P_-^{(i)} e^{ik_{eff}^{(i)}x} \end{Bmatrix} \tag{26}$$

Using the relation $x^{(i+1)b} = x^{(i)b} + d^{(i)}$ and the inverse relation from (26), the interface boundary values of the pressure $p^{(i)}$ and effective velocity $u_{eff}^{(i)}$ at $x^{(i)b}$ are linearly related to those at $x^{(i+1)b}$ through

$$\begin{Bmatrix} p^{(i)}(x^{(i+1)b}) \\ u_{eff}^{(i)}(x^{(i+1)b}) \end{Bmatrix} = \mathbf{B}_{(i)} \begin{bmatrix} e^{-ik_{eff}^{(i)}d^{(i)}} & 0 \\ 0 & e^{ik_{eff}^{(i)}d^{(i)}} \end{bmatrix} \begin{Bmatrix} P_+^{(i)} e^{-ik_{eff}^{(i)}x^{(i)}} \\ P_-^{(i)} e^{ik_{eff}^{(i)}x^{(i)}} \end{Bmatrix} = \mathbf{B}_{(i)}\mathbf{D}(d^{(i)}) \begin{Bmatrix} P_+^{(i)} e^{-ik_{eff}^{(i)}x^{(i)}} \\ P_-^{(i)} e^{ik_{eff}^{(i)}x^{(i)}} \end{Bmatrix}$$

$$= \mathbf{B}_{(i)}\mathbf{D}(d^{(i)})[\mathbf{B}_{(i)}]^{-1} \begin{Bmatrix} p^{(i)}(x^{(i)b}) \\ u_{eff}^{(i)}(x^{(i)b}) \end{Bmatrix} = \mathbf{T}_{(i)} \begin{Bmatrix} p^{(i)}(x^{(i)b}) \\ u_{eff}^{(i)}(x^{(i)b}) \end{Bmatrix} \tag{27}$$

where $\mathbf{T}_{(i)}$ is the 2×2 acoustic transfer matrix for the ith layer and is defined as the following form:

$$\mathbf{T}_{(i)} = \mathbf{B}_{(i)}\mathbf{D}(d^{(i)})[\mathbf{B}_{(i)}]^{-1} = \frac{1}{2} \begin{bmatrix} e^{-i(k_{eff}^{(i)}d^{(i)})} + e^{i(k_{eff}^{(i)}d^{(i)})} & Z_{eff}^{(i)}[e^{-i(k_{eff}^{(i)}d^{(i)})} - e^{i(k_{eff}^{(i)}d^{(i)})}] \\ \dfrac{1}{Z_{eff}^{(i)}}[e^{-i(k_{eff}^{(i)}d^{(i)})} - e^{i(k_{eff}^{(i)}d^{(i)})}] & e^{-i(k_{eff}^{(i)}d^{(i)})} + e^{i(k_{eff}^{(i)}d^{(i)})} \end{bmatrix} \tag{28}$$

Since the construction of the acoustic transfer matrix $\mathbf{T}_{(i)}$ is valid for any arbitrary layer in a mesoscopic unit cell, one can obtain the complete acoustic transfer matrix $\mathbf{T}$ for the n layered mesoscopic unit cell containing n different porous acoustic materials (see Fig. 2). Extending the above result (28) in the iteration process, the pressure and effective velocity at the left boundary ($x^{(1)b}$) of the 1th layer are related to those at the right boundary ($x^{(n+1)b}$) of the nth layer by

$$\begin{Bmatrix} p^{(n)}(x^{(n+1)b}) \\ u_{eff}^{(n)}(x^{(n+1)b}) \end{Bmatrix} = \mathbf{T} \begin{Bmatrix} p^{(1)}(x^{(1)b}) \\ u_{eff}^{(1)}(x^{(1)b}) \end{Bmatrix} \tag{29}$$

where

$$\mathbf{T} = \mathbf{T}^{(n)}\mathbf{T}^{(n-1)} \cdots \mathbf{T}^{(1)} \tag{30}$$

Here $\mathbf{T}$ will be denoted as the accumulated acoustic transfer matrix with $d = d^{(1)} + d^{(2)} + \cdots + d^{(n)}$ at the meso-scale level.

Let us now consider the acoustic composite structure composed of an infinite repetition of a single n layered mesoscopic unit cell. To do this, we may invoke the Floquet–Bloch theorem that relates the harmonic response at a given point in a unit cell to the corresponding point in an adjacent one, yielding

$$\begin{Bmatrix} p^{(i)}(x+d) \\ u_{eff}^{(i)}(x+d) \end{Bmatrix} = \mathrm{e}^{-\mathrm{i}qd} \begin{Bmatrix} p^{(i)}(x) \\ u_{eff}^{(i)}(x) \end{Bmatrix} \tag{31}$$

where q is the wave number corresponding to the macroscopic wave field across the periodic structure. Substituting (31) into (29), the following eigen-value problem is given:

$$[\mathbf{T}-\mathbf{I}\mathrm{e}^{-\mathrm{i}qd}] \begin{Bmatrix} p^{(1)}(x^{(1)b}) \\ u_{eff}^{(1)}(x^{(1)b}) \end{Bmatrix} = \mathbf{0} \tag{32}$$

The solution of (32) appears in complex conjugate pairs and provides dispersion curves for one-directional wave propagation in the infinite multi-periodic acoustic composite structure characterized by the cumulative acoustic transfer matrix $\mathbf{T}$. Finally, one can predict the macro-scale frequency band structure (equivalently the widths and locations of the damping stop- and pass-bands) due to mismatch and multiple layouts of constituent acoustic properties at the meso-scale level.

3.2. Finite periodic case

In the Section 3.1, the ATMM in conjunction with the Floquet–Bloch theorem has been explicited. However, referring the existing literature, one can easily observe that the procedure is only valid for an infinite periodic case. Therefore, another analysis approach is clearly needed for the finite N periodic case. A similar derivation for an elastic composite was previously introduced by Cao and Qi [42] and Hussein et al. [43].

Let us consider a finite acoustic composite structure with periodically N-repeated mesoscopic unit cells, each of unit cell lengths d and n sub-layers, which consist of different rigid porous acoustic materials at the micro-scale level (Fig. 1). Here one can calculate the macroscopic length of the structure as $N_{Layer}=dN$. First, assume that the structure is immersed in a material that has the same properties as those of the first layer in the unit cell (equally, $k_{eff}^{(N_{Layer}+1)}=k_{eff}^{(1)}$ and $Z_{eff}^{(N_{Layer}+1)}=Z_{eff}^{(1)}$). Using the above assumption and the previous result (26), a new acoustic transfer matrix $\overline{\mathbf{T}}_{(i)}$ is redefined as follows:

$$\mathbf{P}_{(i)}=\overline{\mathbf{T}}_{(i)}\mathbf{P}_{(i+1)}, \quad \text{with} \quad \mathbf{P}_{(i)}=\lfloor P_+^{(i)} \;\; P_-^{(i)} \rfloor^{\mathrm{T}} \tag{33}$$

where

$$\overline{\mathbf{T}}_{(i)}=[\mathbf{T}_{(i)}\mathbf{B}_{(i)}\mathbf{C}(x^{(i)b})]^{-1}\mathbf{B}_{(i+1)}\mathbf{C}(x^{(i)b}+d^{(i)})=\frac{1}{2Z_{eff}^{(i+1)}}\begin{bmatrix} (Z_{eff}^{(i)}+Z_{eff}^{(i+1)})\mathrm{e}^{\mathrm{i}(k_{eff}^{(i)}-k_{eff}^{(i+1)})(x^{(i)b}+d^{(i)})} & (-Z_{eff}^{(i)}+Z_{eff}^{(i+1)})\mathrm{e}^{\mathrm{i}(k_{eff}^{(i)}+k_{eff}^{(i+1)})(x^{(i)b}+d^{(i)})} \\ (-Z_{eff}^{(i)}+Z_{eff}^{(i+1)})\mathrm{e}^{-\mathrm{i}(k_{eff}^{(i)}+k_{eff}^{(i+1)})(x^{(i)b}+d^{(i)})} & (Z_{eff}^{(i)}+Z_{eff}^{(i+1)})\mathrm{e}^{-\mathrm{i}(k_{eff}^{(i)}-k_{eff}^{(i+1)})(x^{(i)b}+d^{(i)})} \end{bmatrix} \tag{34}$$

with $\mathbf{C}(x^{(i)b})=diag[\mathrm{e}^{-\mathrm{i}k_{eff}^{(i)}x^{(i)b}},\mathrm{e}^{\mathrm{i}k_{eff}^{(i)}x^{(i)b}}]$. Extending (33) in the iteration process across the structure, the following relationship is derived:

$$\mathbf{P}_{(1)}=[\overline{\mathbf{T}}_{(1)}\overline{\mathbf{T}}_{(2)}\cdots\overline{\mathbf{T}}_{(N_{Layer})}]\mathbf{P}_{(N_{Layer}+1)}=\overline{\mathbf{T}}\mathbf{P}_{(N_{Layer}+1)} \tag{35}$$

with

$$\overline{\mathbf{T}}=\begin{bmatrix} \overline{\mathrm{T}}_{11} & \overline{\mathrm{T}}_{12} \\ \overline{\mathrm{T}}_{21} & \overline{\mathrm{T}}_{22} \end{bmatrix} \tag{36}$$

Here $\mathbf{P}_{(N_{Layer}+1)}$ denotes a vector describing forward and backward traveling wave coefficients in the material that the structure is immersed in. Second, let us consider two types of boundary conditions to estimate (i) a transmission function and (ii) an acoustic absorption coefficient for the structure, respectively. The first type of the associated boundary condition is the absorbing boundary condition [42,43] (or $P_-^{(N_{Layer}+1)}=0$) where waves are not allowed to reflect-back on the right side of the structure, which most published finite TMMs are exclusively based on. Applying the absorbing boundary condition into (35), the frequency-dependent transmission function $H(f)$ is defined:

$$H(f)=\frac{P_+^{(N_{Layer}+1)}\mathrm{e}^{-\mathrm{i}k_{eff}^{(N_{Layer}+1)}Nd}}{P_+^{(1)}}=\frac{1}{\overline{\mathrm{T}}_{11}}\mathrm{e}^{-\mathrm{i}k_{eff}^{(N_{Layer}+1)}Nd} \tag{37}$$

which represents an amplitude and phase relationships between the incident wave at $x^{(1)b}=0$ and the transmitted wave at $x^{(N_{Layer}+1)}=Nd$. On the other hand, different boundary conditions are chosen to elucidate the relationship of the frequency band structure to the acoustic absorption behavior in the structure. Here we use an appropriate set of boundary conditions [15,48–50], which are: (iia) on the region $x^{(1)b}<0$, the structure is in contact with an air of wave number k_0 and impedance

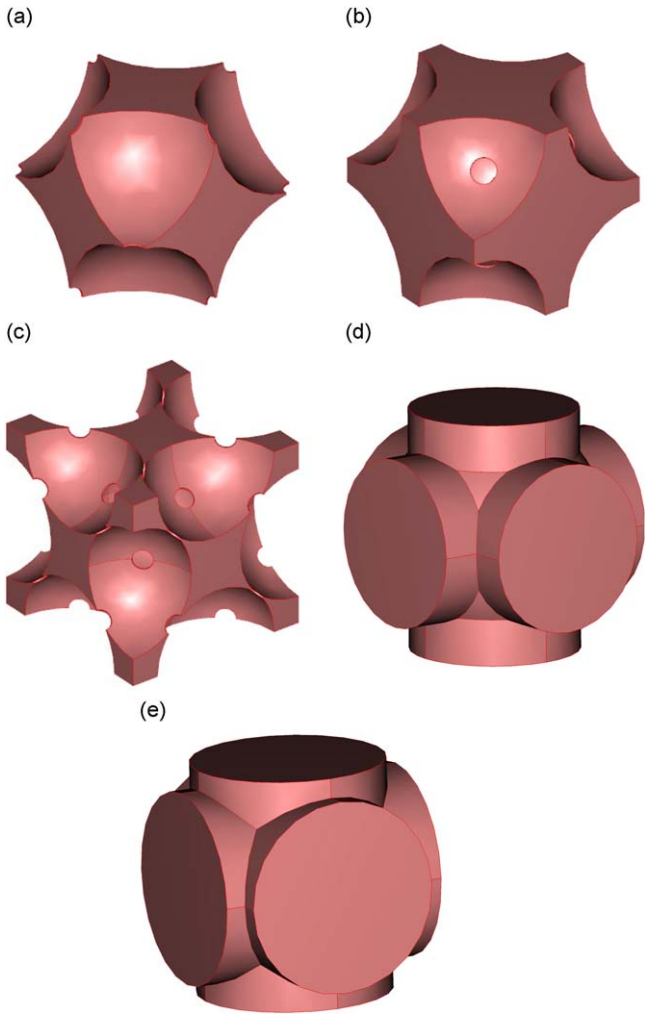

Fig. 3. Three-dimensional unit fluid cell geometries for three close- and two open-packed sphere arrangements: (a) SC-based UFC model, (b) BCC-based UFC model, (c) FCC-based UFC model, (d) opened sphere packing UFC model 1, and (e) open sphere packing UFC model 2.

Table 1
Fluid material properties used in all studies.

ρ_0	T_0	P_0	μ	Pr	γ
1.293 kg/m^3	300 K	10^5 Pa	1.7210^{-5} kg(ms)$^{-1}$	0.715	1.4

Table 2
Statically-estimated parameters for close- and open-packed sphere arrangements considered.

	Closed sphere packing			Opened sphere packing	
	SC	BCC	FCC	OC1	OC2
ϕ	0.476	0.319	0.259	0.668	0.818
$\hat{k}_0$ ($\times 10^{-9}$ kg/m^3)	9.754	2.017	0.672	41.52	85.05
$\hat{k}_0'$ ($\times 10^{-8}$ Pa^{-1})	2.451	0.388	0.268	8.570	16.08
α_0	2.063	2.152	2.458	1.682	1.426
α_0'	1.439	1.353	1.856	1.264	1.199
α_∞	1.397	1.487	1.652	1.317	1.147
Λ ($\times 10^{-3}$ m)	0.378	0.233	0.159	0.267	0.272
Λ' ($\times 10^{-3}$ m)	0.624	0.325	0.247	0.363	0.324

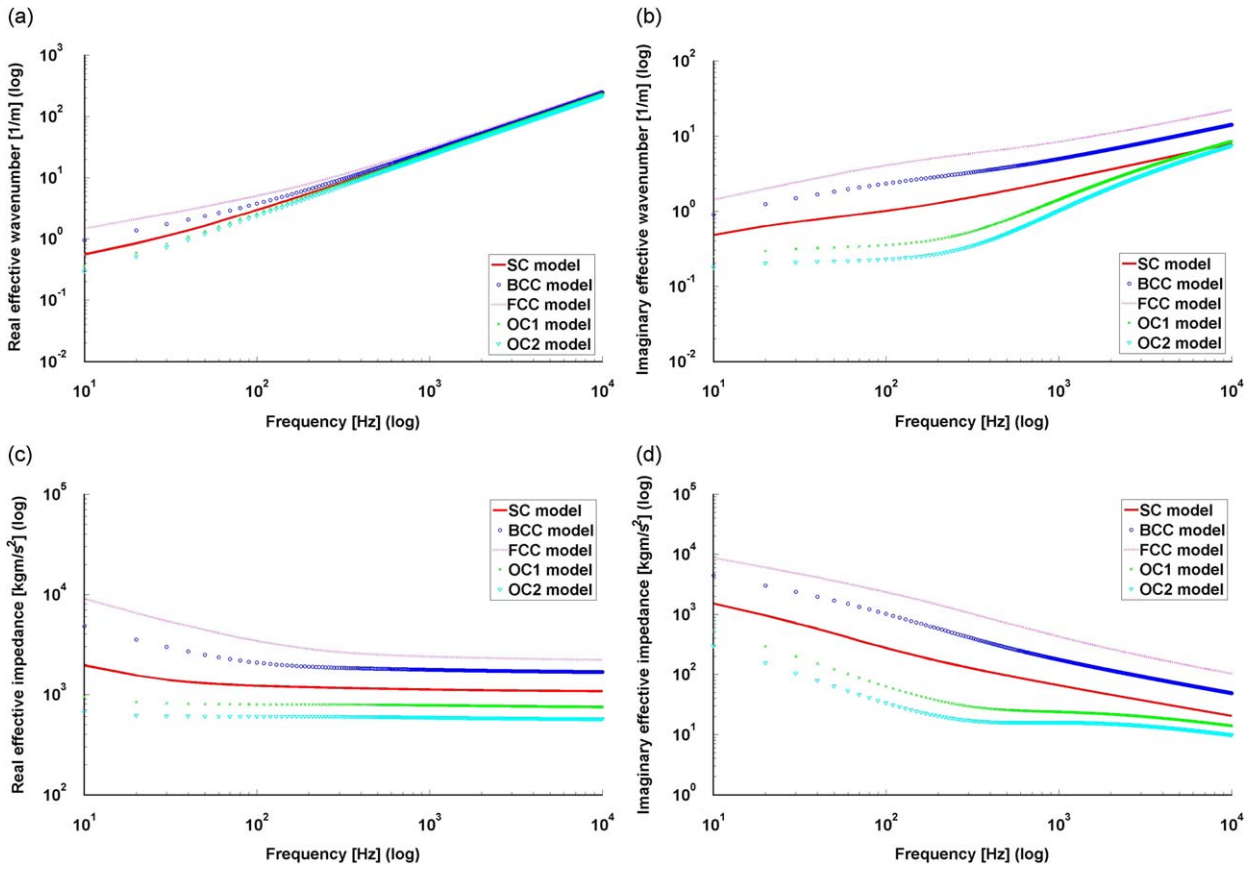

Fig. 4. (a) Real, (b) imaginary parts of the effective wavenumber (k_{eff}) versus frequency, (c) real and (d) imaginary parts of effective impedance (Z_{eff}) versus frequency (based on the hybrid numerical approach).

Z_0 and (iib) at the right end side of the boundary, $x^{(N_{Layer}+1)b}$ waves are allowed to fully reflect back by a rigid impervious wall ($u_{eff}^{(N_{Layer})}(x^{(N_{Layer}+1)b})=0$):

- Boundary condition at $x^{(1)b}$,

$$\begin{aligned} P_+^{(0)}+P_-^{(0)} &= P_+^{(1)}+P_-^{(1)} \\ P_+^{(0)}-P_-^{(0)} &= \frac{Z^{(0)}}{Z_{eff}^{(1)}}(P_+^{(0)}-P_-^{(0)}) \end{aligned} \quad \text{or} \quad \mathbf{P}_{(0)}=\frac{1}{2}\begin{bmatrix} 1+\frac{Z^{(0)}}{Z_{eff}^{(1)}} & 1-\frac{Z^{(0)}}{Z_{eff}^{(1)}} \\ 1-\frac{Z^{(0)}}{Z_{eff}^{(1)}} & 1+\frac{Z^{(0)}}{Z_{eff}^{(1)}} \end{bmatrix}\mathbf{P}_{(1)}=\overline{\mathbf{T}}_{(0)}\mathbf{P}_{(1)} \tag{38}$$

- Boundary condition at $x^{(N_{Layer}+1)b}$,

$$P_+^{(N_{Layer}+1)}e^{-ik_{eff}^{(N_{Layer}+1)}x^{(N_{Layer}+1)b}}=P_-^{(N_{Layer}+1)}e^{ik_{eff}^{(N_{Layer}+1)}x^{(N_{Layer}+1)b}} \tag{39}$$

or

$$\mathbf{P}_{(N_{Layer}+1)}=\begin{bmatrix} 1 & 0 \\ e^{-2ik_{eff}^{(N_{Layer}+1)}x^{(N_{Layer}+1)}} & 0 \end{bmatrix}\mathbf{P}_{(N_{Layer}+1)}=\overline{\mathbf{T}}_{(N_{Layer}+1)}\mathbf{P}_{(N_{Layer}+1)} \tag{40}$$

Associated with boundary conditions (38) and (40), a new acoustic transfer matrix $\overline{\mathbf{T}}^{B}$ is derived as follows:

$$\mathbf{P}_{(0)}=[\overline{\mathbf{T}}_{(0)}\overline{\mathbf{T}}_{(1)}\overline{\mathbf{T}}_{(2)}\cdots\overline{\mathbf{T}}_{(N_{Layer})}\overline{\mathbf{T}}_{(N_{Layer}+1)}]\mathbf{P}_{(N_{Layer}+1)}=\overline{\mathbf{T}}^{B}P_{(N_{Layer}+1)} \tag{41}$$

where

$$\overline{\mathbf{T}}^{B}=\begin{bmatrix} \overline{T}_{11}^{B} & \overline{T}_{12}^{B} \\ \overline{T}_{21}^{B} & \overline{T}_{22}^{B} \end{bmatrix} \tag{42}$$

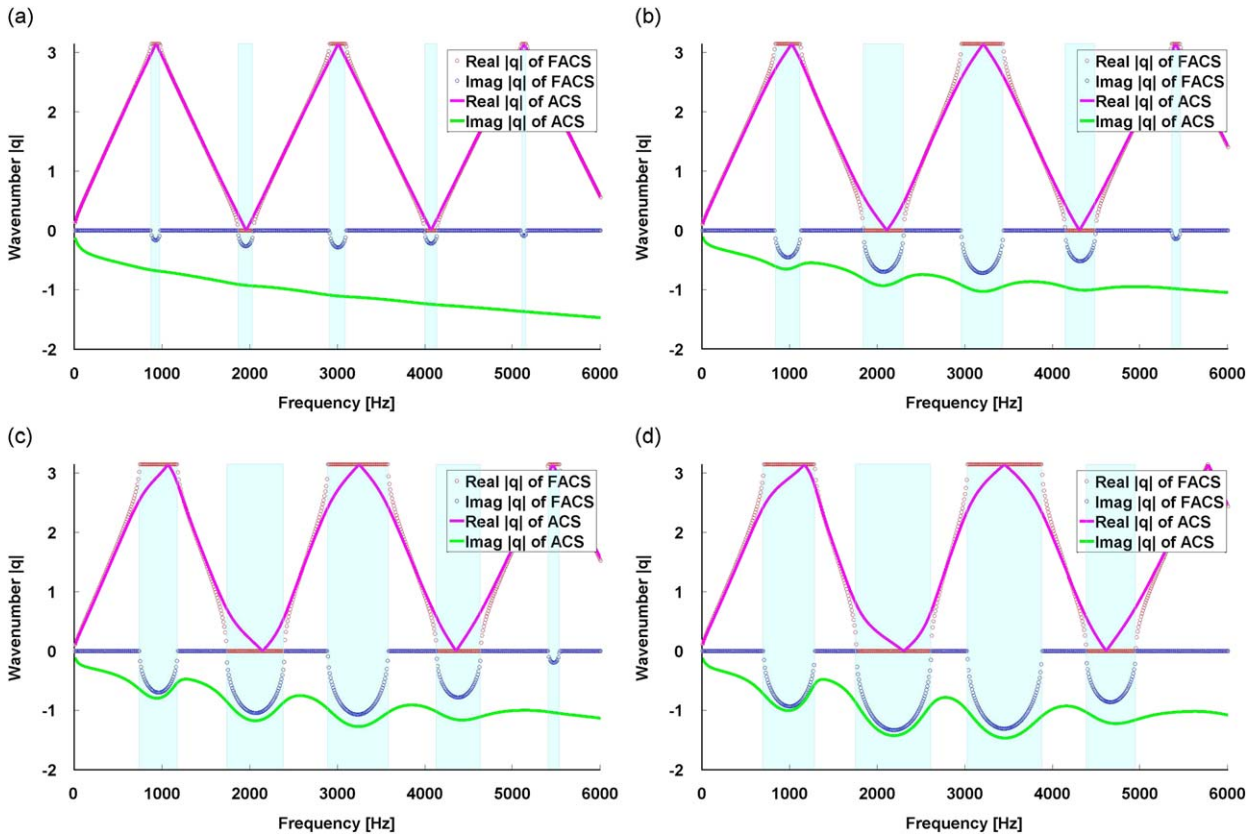

Fig. 5. Real and imaginary parts of frequency-dependent wave numbers |q| for infinite-periodic acoustic composite structures (ACS) and equivalent fictional ones (FACS) with each bi-layer per four mesoscopic unit cells. For convenience, stop bands are shaded: (a) FCC+BCC mesoscopic unit cell, (b) FCC+SC mesoscopic unit cell, (c) FCC+OC1 mesoscopic unit cell, and (d) FCC+OC2 mesoscopic unit cell.

Finally, one can calculate the frequency-dependent acoustic absorption coefficient of the acoustic composite structure as follows:

$$a = 1 - \left| \frac{P_{-}^{(0)}}{P_{+}^{(0)}} \right|^2 \tag{43}$$

4. Numerical results and validations

To implement our numerical formulation, we first calculated static acoustic parameters for five UFC cases, represented by three closed and two opened sphere packing types of porous materials, using the MAM and HNM processes, and then estimated each effective wave number and impedance using (22). These effective variables are used as the meso-scale parameters representing acoustic properties of an arbitrary chosen layer within a mesoscopic unit cell (Section 3). For each packing type, Fig. 3 depicts the irreducible unit fluid cells consisting of the fluid-fluid interstitial space between packed spheres.

Similar to our previous work [29], the radius of the sphere is chosen to be 1 mm and we include a solder joint at each sphere contact point, where the solder radius of the closed packing case is 150 μm and that of the opened packing case is 750 μm ((d) in Fig. 3) and 850 μm ((e) in Fig. 3), respectively. Table 1 provides the coefficients used in the implementation of our approach.

Using the finite element analysis package, COMSOL® Multiphysics, the numerical solutions of the static acoustic parameters ((14) and (15)) are calculated from the decoupled set of three static governing equations and associated boundary conditions on the above representative UFC domain. All parameters are collected in Table 2.

Using the estimated parameters in Table 2 as the input data for Eq. (17), we calculated the effective density and compressibility variables, and then estimated the effective wave number and impedance in a frequency range of interest (here, from 10 to 10,000 Hz), as shown in Fig. 4.

We investigated the macro-scale dispersion relations for four acoustic composite structures composed of bi-layered mesoscopic unit cells using the infinite ATMM. Herein, bi-layered mesoscopic unit cells are defined as two layers of

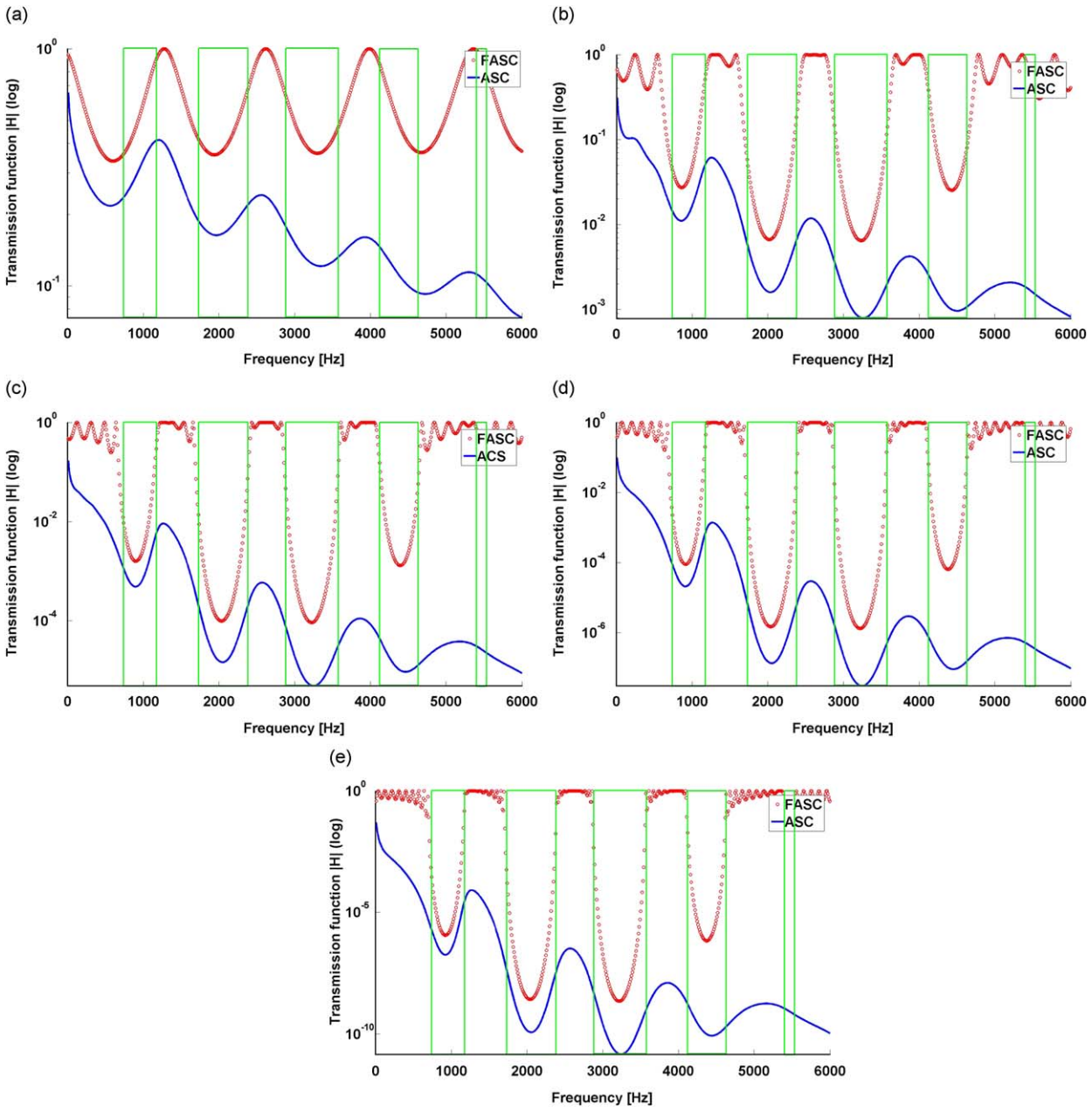

Fig. 6. Frequency-dependent transmission function $|H|$ for the finite structure case composed of 1, 3, 5, 7, and 10 FCC+OC1 mesoscopic unit cells. Stop band regions for the associated infinite case are described by green boxes each figures: (a) 1 repeated FCC+OC1 unit cell, (b) 3 repeated FCC+OC1 unit cell, (c) 5 repeated FCC+OC1 unit cell, (d) 7 repeated FCC+OC1 unit cell, and (e) 10 repeated FCC+OC1 unit cell.

acoustic properties of FCC model with $d^{(1)} = 0.02$ m and one other layer (SC, BCC, OC1, or OC2 model) with $d^{(2)} = 0.1$ m. Fig. 5 provides the frequency band structures in infinite-periodic acoustic composite structures in a frequency range of $10 \le f \le 6,000$ Hz for wave numbers falling in the first Brillouin zone [51], i.e., $0 \le q \le \pi$. Real-valued wave numbers are associated with pass-band modes, while the imaginary-valued ones correspond to stop-band modes. For purposes of comparison, we also considered fictional acoustic composite structures (FACS) having no imaginary parts of effective density and compressibility parameters-equally, no attenuation effects.

As can be seen in Fig. 5, the ACS composed of the FCC+OC2 bi-layered mesoscopic unit cell demonstrates the widest stop-bands as compared to the other bi-layered materials. This is due to the high mismatch between constituent acoustic properties. Moreover, unlike the distinct resonance appearances in the fictional ACS, one can observe that the introduction of the real materials' attenuation effects enhances the anti-resonances due to damping.

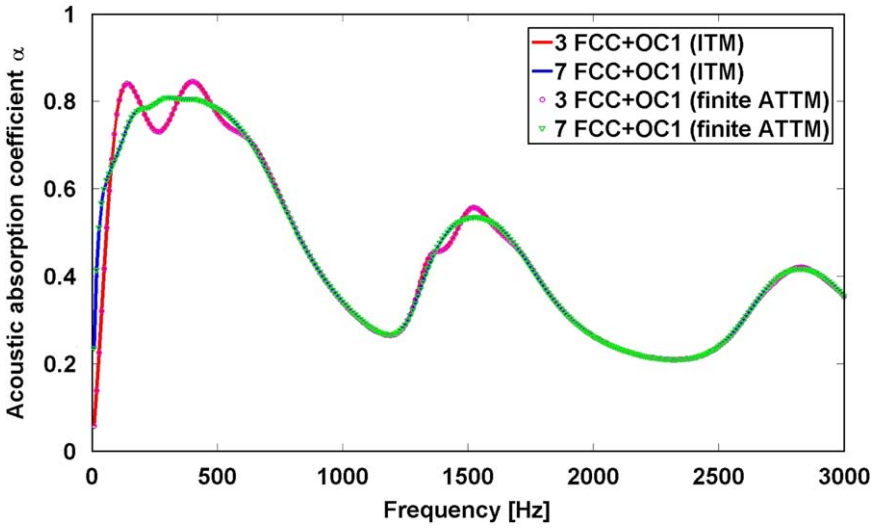

Fig. 7. Comparison of acoustic absorption coefficients from finite ATMM and ITM via frequency.

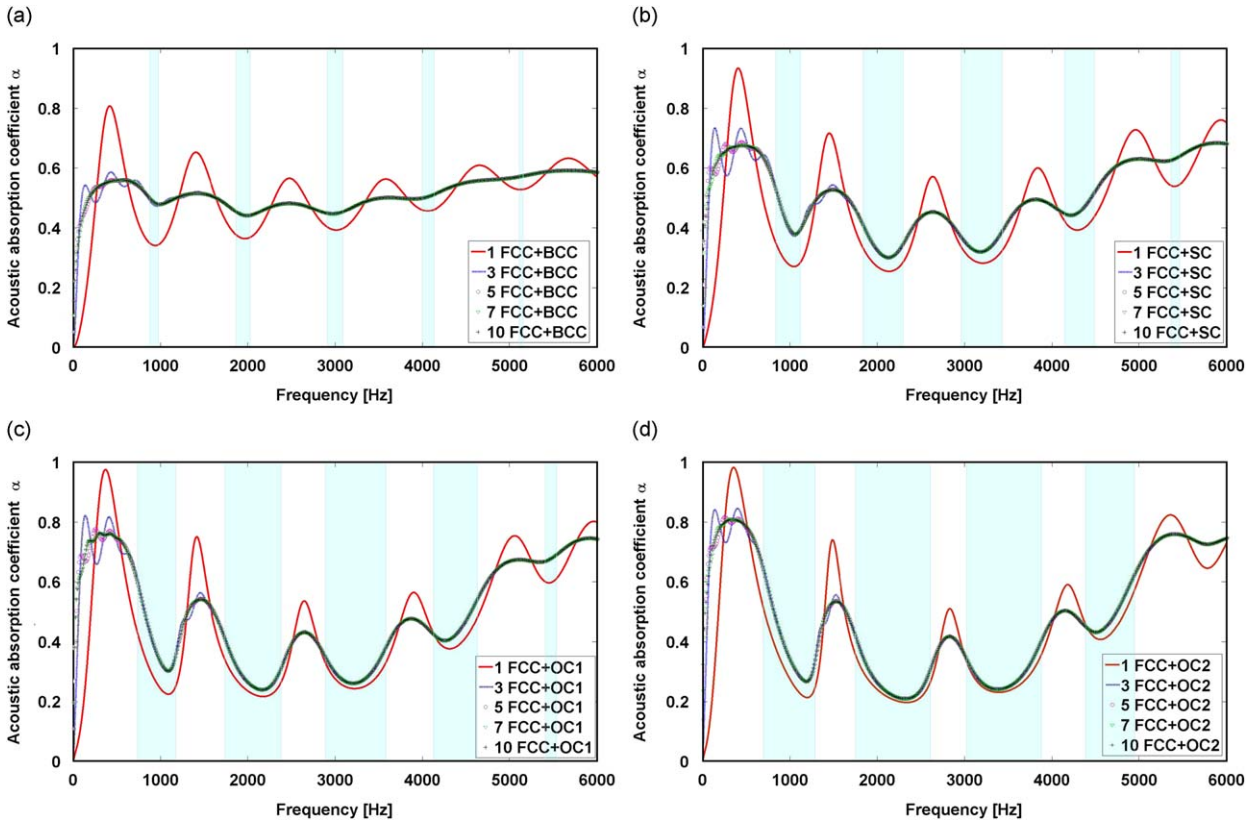

Fig. 8. Frequency-dependent acoustic absorption coefficients α for the finite ACSs composed of 1, 3, 5, 7, and 10 four bi-layered mesoscopic unit cells. Stop band regions for the corresponding infinite ones are shaded: (a) finite ACS with FCC+BCC unit cells, (b) finite ACS with FCC+SC unit cells, (c) finite ACS with FCC+OC1 unit cells, and (d) finite ACS with FCC+OC2 unit cells.

To assess the validity of estimated dispersion relations, we choose the validation process used in the ETMM to investigate the finiteness effects on the frequency band structure [42,43]. Fig. 6 shows the frequency-dependent transmission function $|H|$ of the finite ACS composed of FCC+OC1 bi-layered mesoscopic unit cell as a function of the repeated number $N = 1, 3, 5, 7, 10$.

For comparison purposes, we also plot the corresponding finite FACS. As one can see, for the structures composed of 1 and 3 finite-periodic unit cells, the damped frequency band structure does not match well with those of the infinite-periodic unit cell. However, in finite ACS made of at least 5 repeated unit cells, the general shape of the transmission function closely agrees with the damped frequency band width and location of the infinite one. This result implies that the transmission response predictions for a finite composite can be appropriately predicted from the associated infinite one.

We next investigate the relationship between acoustic absorption behavior and frequency band structure in multi-periodic acoustic composite structures using the finite ATMM. To do so, we calculate the frequency-dependent acoustic absorption coefficients α for the four cases of the finite ACS composed of four bi-layered mesoscopic unit cells with the repeated numbers $N=1,3,5,7,10$. We consider the 3 and 7 repeated FCC+OC1 unit cell cases to demonstrate the validity of the finite ATTM with (38) and (40) by comparing our numerical results with the traditional absorption curves calculated from the ITM [15,48–50], as shown in Fig. 7.

As can be seen in Fig. 7, the frequency-dependent acoustic absorption coefficients obtained from both approaches are in close agreement in the frequency range of interest. Moreover, this result elucidates the close relationship between acoustic absorption and frequency band structure. To validate and test this link, the acoustic absorption coefficient α, given in Eq. (43), is estimated for the finite structure with $N=1,3,5,7,10$ over the same frequency range considered in Fig. 5, and the results are illustrated in Fig. 8. For convenience, stop band regions for the corresponding infinite cases are also shaded.

As the repeated number N of a unit cell increases, each shape of four acoustic absorption coefficients closely agree with the frequency band width and location of the corresponding infinite ACS. This result is consistent with the previous result regarding the transmission functions behaviors in a frequency range of interest (Fig. 6). The close relationship of the damped frequency band structure to the acoustic absorption behavior of the finite acoustic composite structure brings rise to the conclusion that the finite acoustic composite structure can be designed for both a desired band structure (e.g., desired stop bands) as well as for efficient acoustic absorption using the techniques developed herein.

5. Conclusion

In conclusion, the wave propagation behavior in multi-periodic acoustic composite structures has been investigated with the aim of predicting and controlling their dispersion behavior. Infinite and finite acoustic transfer matrix methods have been illustrated which yield damped frequency band structure and associated acoustic absorption curves. Several examples are numerically evaluated using four periodic porous media as basic building blocks. We have compared the general shapes of acoustic absorption curves for the finite periodic cases with frequency band structures for the corresponding infinite ones, and established a general guideline that five or more unit cells are needed to justify the use of an infinite transfer matrix. Using mismatch and multiple layouts of constituent acoustic properties and thicknesses inside arbitrary meso-scale unit cells, it is shown on the examples how the extents of pass- and stop-bands can be optimized to some extent. We have also explored the close relationship between acoustic absorption and frequency band structure. Follow-on work may consider systematically designing acoustic composite structures, using the analysis tools presented, for use in acoustic waveguide and filter applications.

Acknowledgments

The authors gratefully acknowledge the EADS N.A. Foundation's support of this work. They are also deeply thankful to Denis Lafarge for very fruitful discussions and comments during review of the paper.

References

[1] L.J. Gibson, M.F. Ashby, *Cellular Solids: Structure and Properties*, Cambridges University Press, UK, 1999.
[2] G. Kirchhoff, Über den einfluß der wärmeleitung in einem gase auf die schallbewegung, *Annual Review of Physical Chemistry* 134 (1868) 177–193.
[3] M.A. Biot, Theory of propagation of elastic waves in a fluid saturated porous solid I: low-frequency range, *Journal of the Acoustical Society of America* 28 (2) (1956) 168–178.
[4] A. Bensoussan, J.L. Lions, G. Papanicolaou, *Asymptotic Analysis for Periodic Structures*, North-Holland, Amsterdam, 1978.
[5] E. Sanchez-Palencia, *Non-Homogeneous Media and Vibration Theory*, Springer-Verlag, Berlin, 1980.
[6] J.L. Auriault, Dynamic behaviour of a porous media saturated by a Newtonian fluid, *International Journal of Engineering Science* 18 (1980) 775–785.
[7] R. Burridge, J.B. Keller, Poroelasticity equations derived from microstructure, *Journal of the Acoustical Society of America* 70 (4) (1981) 1140–1146.
[8] J.L. Auriault, L. Borne, R. Chambon, Dynamics of porous saturated media, checking of the generalized law of Darcy, *Journal of the Acoustical Society of America* 77 (5) (1985) 1641–1650.
[9] D.L. Johnson, J. Koplik, R. Dashen, Theory of dynamic permeability and tortuosity in fluid-saturated porous media, *Journal of Fluid Mechanics* 176 (1987) 379–402.
[10] P. Sheng, M.Y. Zhou, Dynamic permeability in porous media, *Physical Review Letter* 61 (14) (1988) 1591–1594.
[11] A.N. Norris, On the viscodynamic operator in Biot's equations of poroelasticity, *Journal of Wave-Material Interaction* 1 (4) (1986) 365–380.
[12] M.Y. Zhou, P. Sheng, First-principles calculations of dynamic permeability in porous media, *Physical Review B* 39 (16) (1989) 12027–12039.
[13] Y. Champoux, J.F. Allard, Dynamic tortuosity and bulk modulus in air-saturated porous media, *Journal of Applied Physics* 70 (1991) 1975–1979.
[14] D.M.J. Smeulders, R.L.G.M. Eggels, M.E.H. Van Dongen, Dynamic permeability: reformulation of theory and new experimental and numerical data, *Journal of Fluid Mechanics* 245 (1992) 211–227.
[15] J.-F. Allard, *Propagation of Sound in Porous Media*, Elsevier Applied Science, Amsterdam, 1993.
[16] S.R. Pride, F.D. Morgan, A.F. Gangi, Drag forces of porous medium acoustics, *Physical Review B* 47 (9) (1993) 4964–4978.

[17] D. Lafarge, Propagation du son dans les matériaux poreux à structure rigide saturés par un fluide viscothermique, PhD Thesis, Université du Maine, 1993.
[18] D. Lafarge, P. Lemarinier, J.F. Allard, Dynamic compressibility of air in porous structures at audible frequencies, *Journal of the Acoustical Society of America* 102 (4) (1997) 1995–2006.
[19] C. Boutin, P. Royer, J.L. Auriault, Acoustic absorption of porous surfacing with dual porosity, *International Journal of Solids and Structures* 35 (1998) 4709–4737.
[20] J.G. Berryman, Comparison of upscaling methods in poroelasticity and its generalizations, *Journal of Engineering Mechanics* 131 (9) (2005) 928–936.
[21] C. Boutin, Rayleigh scattering of acoustic waves in rigid porous media, *Journal of the Acoustical Society of America* 122 (4) (2007) 1888–1905.
[22] A.M. Chapman, J.J.L. Higdon, Oscillatory Stokes flow in periodic porous media, *Physics of Fluids A: Fluid Dynamics* 4 (1992) 2099–2116.
[23] L. Borne, Harmonic Stokes flow through periodic porous media: a 3D boundary element method, *Journal of Computational Physics* 99 (2) (1992) 214–232.
[24] A. Cortis, Dynamic Acoustic Parameters of Porous Media: A Theoretical, Numerical and Experimental Investigation, PhD Thesis, Delft Unviersity Press, 2003.
[25] S. Gasser, F. Paun, Y. Bréchet, Absorptive properties of rigid porous media: application to face centered cubic sphere packing, *Journal of the Acoustical Society of America* 117 (4) (2005) 2090–2099.
[26] K. Schladitz, S. Peters, D. Reinel-Bitzer, A. Wiegmann, J. Ohser, Design of acoustic trim based on geometric modeling and flow simulation for non-woven, *Computational Materials Science* 38 (1) (2006) 56–66.
[27] C. Perrot, F. Chevillotte, R. Panneton, Dynamic viscous permeability of an open-cell aluminum foam: computations versus experiments, *Journal of Applied Physics* 103 (2008) 024909.
[28] C. Perrot, F. Chevillotte, R. Panneton, Bottom-up approach for microstructure optimization of sound absorbing materials, *Journal of the Acoustical Society of America* 124 (2) (2008) 940–948.
[29] C.-Y. Lee, M.J. Leamy, J.H. Nadler, Acoustic absorption calculation in irreducible porous media: a unified computational approach, *Journal of the Acoustical Society of America* 126 (4) (2009) 1862–1870.
[30] G. Floquet, Sur les Équations Différentielles Linéaries à Coefficients Périodiques, *Annales de l'Ecole Normale Supérieur* 12 (1883) 47–88.
[31] F. Bloch, Über die Quantenmechanik der Electron in Kristallgittern, *Zeitschrift für Physik* 52 (1928) 555–600.
[32] W.T. Thomson, Transmission of elastic waves through a stratified medium, *Journal of Applied Physics* 21 (2) (1950) 89–93.
[33] N.A. Habkell, The dispersion of surface waves on multilayered media, *Bulletin of the Seismological Society of America* 43 (1) (1953) 17–34.
[34] E. Yablonovitch, Photonic band-gap crystals, *Journal of Physics: Condensed Matter* 5 (1993) 2443–2460.
[35] T. Miyashita, Sonic crystals and sonic wave-guides, *Measurement Science and Technology* 16 (2005) R47–R63.
[36] M. Sigalas, M.S. Kushwaha, E.N. Economou, M. Kafesaki, M.I.E. Psarobas, W.S. Chevillotte, Classical vibrational modes in phononic lattices: theory and experiment, *Zeitschrift für Kristallographie* 220 (2005) 765–809.
[37] W.M. Ewing, W.S. Jardetzky, F. Press, *Elastic Waves in Layered Media*, McGraw-Hill, New York, 1957.
[38] L.M. Brekhovskikh, *Waves in Layered Media*, second ed., Acadamic Press, New York, 1980.
[39] P. Cervenka, P. Challande, A new efficient algorithm to compute the exact reflection and transmission factors for plane waves in layered absorbing media (liquids and solids), *Journal of the Acoustical Socity of America* 89 (41) (1991) 1579–1589.
[40] R. Esquivel-Sirvent, G.H. Cocoletzi, Band structure for the propagation of elastic waves in superlattices, *Journal of the Acoustical Society of America* 95 (1) (1994) 86–90.
[41] B. Brouard, D. Lafarge, J.-F. Allard, A general method of modeling sound propagation in layered media, *Journal of Sound and Vibration* 183 (1) (1995) 129–142.
[42] W. Cao, W. Qi, Plane wave propagation in finite 2-2 composites, *Journal of Applied Physics* 78 (1995) 4627–4632.
[43] M.I. Hussein, G.M. Hulbert, R.A. Scott, Dispersive elastodynamics of 1D banded materials and structures: analysis, *Journal of Sound and Vibration* 289 (4–5) (2006) 779–806.
[44] B. Merheb, P.A. Deymier, M. Jain, et al., Elastic and viscoelastic effects in rubber/air acoustic band gap structures: a theoretical and experimental study, *Journal of Applied Physics* 104 (6) (2008) 064913.
[45] B. Merheb, P.A. Deymier, K. Muralidharan, et al., Viscoelastic effect on acoustic band gaps in polymer-fluid composites, *Modeling and Simulation in Materials Science and Engineering* 17 (7) (2009) 075013.
[46] R.J.S. Brown, Connection between formation factor for electrical resistivity and fluid–solid coupling factor in Biot equations for acoustic waves in fluid-filled porous media, *Geophysics* 45 (1980) 1269–1275.
[47] S. Torquato, Relationship between permeability and diffusion-controlled trapping constant of porous media, *Physical Review Letters* 64 (22) (1990) 2644–2646.
[48] C. Zwikker, C.W. Kosten, *Sound Absorbing Materials*, Elsevier, New York, 1949.
[49] S. Gasser, Etude des propriétés acoustiques et mécaniques d'un matériau métallique poreux modèle à base de spheres creuses de nickel, PhD Thesis, INPG, 2003.
[50] N. Auffray, R. Bouchet, Y. Bréchet, Modèles d'acoustique phénoménologiques—Application à la conception de matériau sur mesure, *18ème Congrès Français de Mécanique*, Grenoble, 27–31 août, 2007.
[51] L. Brillouin, *Wave Propagation in Periodic Structures*, second ed., Dover Publication, New York, 1953.
[52] M. Bruneau, C. Potel, *Materials and Acoustics Handbook*, Wiley-ISTE, 2009.